University of Groningen

Characterization of organic semiconductors and optoelectronic elements

Melzer, Christian

IMPORTANT NOTE: You are advised to consult the publisher's version (publisher's PDF) if you wish to cite from it. Please check the document version below.

Document Version
Publisher's PDF, also known as Version of record

Publication date:
2004

Link to publication in University of Groningen/UMCG research database

Citation for published version (APA):
Melzer, C. (2004). *Characterization of organic semiconductors and optoelectronic elements*. s.n.

Copyright
Other than for strictly personal use, it is not permitted to download or to forward/distribute the text or part of it without the consent of the author(s) and/or copyright holder(s), unless the work is under an open content license (like Creative Commons).

The publication may also be distributed here under the terms of Article 25fa of the Dutch Copyright Act, indicated by the "Taverne" license. More information can be found on the University of Groningen website: https://www.rug.nl/library/open-access/self-archiving-pure/taverne-amendment.

Take-down policy
If you believe that this document breaches copyright please contact us providing details, and we will remove access to the work immediately and investigate your claim.

Downloaded from the University of Groningen/UMCG research database (Pure): http://www.rug.nl/research/portal. For technical reasons the number of authors shown on this cover page is limited to 10 maximum.

Download date: 04-06-2022

7

Organic donor/acceptor photovoltaics

Abstract

In this chapter, the influence of the film organization of the donor/acceptor system on the cell performance of organic photovoltaic cells is discussed with a focus on characteristic parameters, such as the open circuit voltage (U_{oc}) and the photovoltaic sensitivity. At first, the photovoltaic properties of double-layer cells with one single planar heterojunction are compared with those of cells based on a blend of the same donor and acceptor materials, containing a spatially distributed heterojunction interface. In particular, we emphasize the impact of interface effects on U_{oc} and suggest a simple dilution model, which provides a link between the film morphology and U_{oc}. The influence of the film morphology on the susceptible volume fraction for efficient exciton dissociation is discussed. Secondly, we report on the action spectra of double-layer cells, which provide information on the exciton diffusion length of the employed materials. Finally, results on the morphology of thin films based on a donor/acceptor diblock copolymer are presented. The revealed film organization is compared to the photoresponse of corresponding photovoltaic cells.

7.1 Introduction

In the last decade, the potential of organic materials in the field of electronics triggered novel interest in material sciences, chemistry and physics. While organic light-emitting diodes are already commercially available, efficiencies of organic solar cells do not yet fulfill the industrial demands [1-6]. This requires an intensive search for more efficient organic materials suitable for photovoltaic applications, and a better understanding of the cell physics.

The photovoltaic effect involves the creation of electrons and holes under optical excitation and their successive collection at opposite electrodes. Upon excitation of organic semiconductors by light, neutral electron/hole pairs are created, called excitons [7]. The mobile excitons, having a lifetime in the sub-nanosecond range [8, 9], diffuse through the organic medium until they relax and the photogenerated charges get lost for the photovoltaic effect. In order to make electrons and holes available for the external circuit, excitons have to dissociate. Dissociation efficiently occurs at the interface of two materials with different ionization potentials and electron affinities, leading to the common use of donor/acceptor-type photovoltaic systems [1, 2, 10]. The energy of an optically excited donor electron is lowered by its ultra-fast transfer (sub-picosecond range) to the lowest unoccupied molecular orbital (LUMO) of the acceptor. This reversible metastable electron transfer results in electrons and holes that are susceptible for further transport. By using metal electrodes with different workfunctions (φ), a built-in field is created, leading to an electron current along the acceptor phase towards the low-workfunction metal and a hole current along the donor phase towards the high-workfunction electrode.

The quality of photovoltaic cells is reflected by a number of characteristics that can be obtained by current-voltage (IV) measurements performed under illumination. At zero bias, the photovoltaic performance is characterized by the photovoltaic sensitivity (S), which is the photocurrent density (short circuit condition) divided by the light intensity. The open circuit voltage (U_{oc}) is the required bias, at which no current is measured under illumination: the dark current and the photocurrent are equal in amplitude, but proceed in opposite directions. Usually, U_{oc} is close to the built-in potential (U_{bi}). The diode quality is characterized by the fill factor (FF), which is the maximal electrical power over the product of U_{oc} and the short circuit current. Finally, the external power conversion efficiency (η) of the photovoltaic cell is defined as the electrical output power divided by the input power of the light. Hence, η is equal to the product of S, FF, and U_{oc}. The definitions of the photovoltaic characteristics are listed in Table. 7.1.

Currently, two basic donor/acceptor cell structures are mainly discussed displaying contrary advantages and drawbacks. Double-layer cell structures with a single planar heterojunction interface show good diode behavior, but the limited exciton dissociation interface causes a rather low sensitivity [3, 11, 12]. In this respect, a percolated system of donor and acceptor phases, i.e. a network of heterojunctions through the entire film, seems to be more promising [1, 2, 5]. In turn, however, charge

carrier transport in this second device structure might be less efficient due to the intermixing of two different materials. Consequently, internal losses of photogenerated charge carriers might become more essential, which would eventually restrict the photovoltaic response of a percolated photovoltaic cell. It is thus not evident whether a photovoltaic system based on a blend of donor and acceptor materials is superior if compared to a double-layer system of the same compounds. Since the morphology of the active layer in an organic donor/acceptor photovoltaic cell is obviously of crucial importance for an efficient cell performance, it is subject of this chapter.

7.2 Photovoltaic performance and morphology

In this section, the impact of the morphology of the donor/acceptor system on the overall photovoltaic cell performance is discussed. As photovoltaic model systems, we compared the two extreme structures of a strict double-layer and a random blend organization of donor and acceptor materials. For both film structures, the same materials and identical preparation procedures were employed, in order to address exclusively the impact of the morphology on the cell performance. As the anode, we used indium tin oxide (ITO) covered with a thin layer of poly(3,4-ethylene dioxythiophene) that was highly doped with poly(styrene sulfonic acid) (PEDOT:PSS), while aluminum (Al) was employed as the cathode. Pre-patterned ITO-coated glass substrates were wet cleaned and a thin layer (~80 nm) of PEDOT:PSS (Bytron P) was deposited by spin-coating. The layer was dried under high vacuum at elevated temperature. Double-layer cells were prepared by consecutive thermal vacuum deposition of the donor (*E*,*E*,*E*,*E*)-1,4-bis[(4-styryl)styryl]-2-methoxy-5-(2'-ethyl-hexyloxy)benzene (MEH-OPV5) and the acceptor Buckminster fullerene (C_{60}), while bulk heterojunction photovoltaic cells were obtained by the co-deposition of both

Characteristic	Definition
Short circuit current	$I \equiv I_{sc}$ for $U = 0$
Open circuit voltage	$U \equiv U_{oc}$ for $I = 0$
Photovoltaic sensitivity	$S \equiv \frac{I_{sc}}{P_L}$
Fill factor	$FF \equiv \frac{(I \times U)_{max}}{I_{sc} U_{oc}}$
External power conversion efficiency	$\eta \equiv \frac{(I \times U)_{max}}{P_L} = S \cdot FF \cdot U_{oc}$

Table 7.1 Photovoltaic characteristics of cells under illumination. I, U and P_L are the current, the applied voltage, and the light power, respectively.

moieties in a 1:1 ratio (1 Å/s at 10^{-6} mbar). The substrate temperature was equal to room temperature during deposition. Subsequently, Al was vacuum-deposited at 10^{-6} mbar on the obtained structures. All measurements were performed in an inert environment.

In Fig. 7.1, the IV–curves of an ITO/PEDOT:PSS/MEH-OPV5/C_{60}/Al double-layer cell in the dark and under illumination are presented. The cell showed an S of around 0.054 A/W and a high FF of 0.45. With U_{oc} = 0.88 V, this resulted in a monochromatic η of ~ 2 % (illuminated at 458 nm with 1mW/cm^2). S was constant over a broad range of light intensity (P_L), and U_{oc} saturated to almost 1 V at a P_L of approximately 10 mW/cm^2 (Fig. 7.2). A saturated open circuit voltage (U_{soc}) of 0.9 ±0.1 V was found as the average of several samples.

S of an ITO/PEDOT:PSS/MEH-OPV5+C_{60}/Al co-deposited cell was measured to be 0.078 A/W (Fig. 7.1, λ = 458 nm, P_L = 1 mW/cm^2). At low P_L (< 0.1 mW/cm^2), S was about 0.1 A/W, which is twice higher than for double-layer cells, and decreased with an increase in P_L. The FF of the co-deposited cell was determined to be only 0.25, and U_{oc} was found to be 0.65 V. U_{oc} saturated to 0.7 ±0.1 V at high P_L, averaged over several samples.

In Table 7.2, the photovoltaic parameters obtained for consecutively and co-deposited cells are summarized [13]. It is apparent that the higher photovoltaic sensitivity of co-deposited cells is negatively compensated by their lower FF and U_{oc}. This results in a monochromatic external power conversion efficiency of 1 % that is,

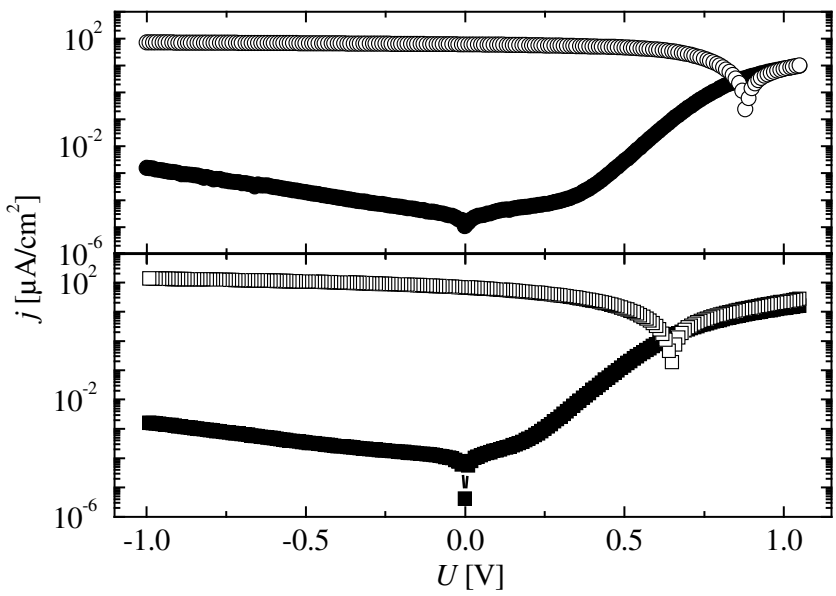

Figure 7.1 IV–characteristics of double-layer ITO/PEDOT:PSS/MEH-OPV5/C_{60}/Al (top) and of co-deposited ITO/PEDOT:PSS/MEH-OPV5 + C_{60}/Al cells (bottom) in the dark (filled symbols) and under illumination (open symbols) with 1 mW/cm^2 at 458 nm. The total layer thickness was around 100 nm in both cases.

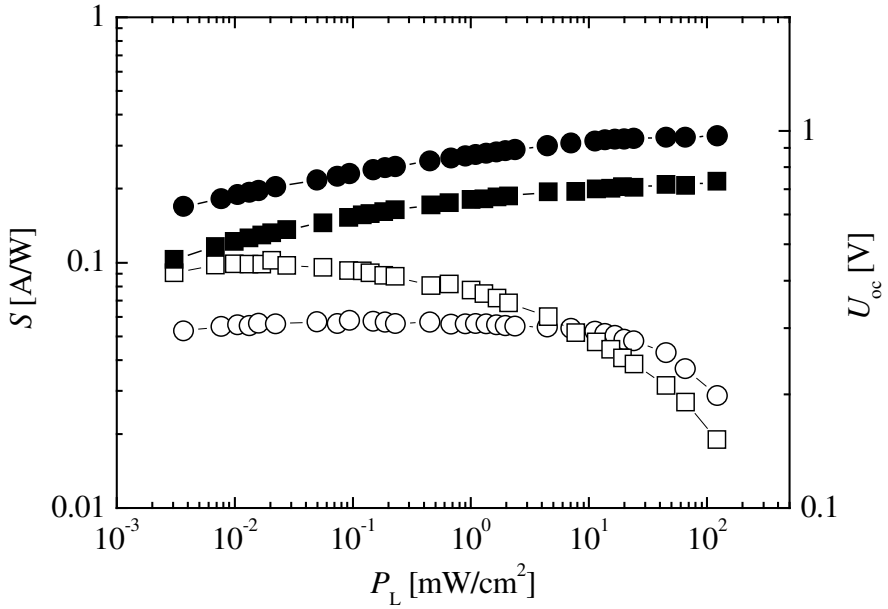

Figure 7.2 Photovoltaic sensitivity (open symbols) and open circuit voltage (filled symbols) versus the light intensity for the consecutively (circles) and co-deposited cells (squares) of Fig. 7.1.

	S [A/W]	FF	U_{oc} [V]	η [%]	U_{soc} [V]	δU_{bi} [eV]	N_i [10^{16} cm^{-3}]	W_{0V} [nm]
Double-layer	0.054	0.45	0.88	2.1	0.9 ±0.1	0.0 ±0.1	–	–
Blend	0.078	0.25	0.65	1.3	0.7 ±0.1	-0.2 ±0.1	0.5 ±0.1	240 ±7
Single-layer MEH-OPV5	–	–	–	–	1.1 ±0.1	0.2 ±0.1	–	–
Single-layer C_{60}	–	–	–	–	0.3 ±0.2	-0.6 ±0.2	1.1 ±0.4	110 ±20

Table 7.2 Main cell characteristics for double-layer ITO/PEDOT:PSS/MEH-OPV5/C_{60}/Al cells, co-deposited ITO/PEDOT:PSS/MEH-OPV5 + C_{60}/Al cells, single-layer MEH-OPV5, and C_{60} cells. The total thickness of the semiconducting layers was ~100 nm. S is the photovoltaic sensitivity and FF is the fill factor measured with 1 mW/cm^2 light intensity at an illumination wavelength of 458 nm. U_{soc} is the saturated open circuit voltage at the same wavelength, and δU_{bi} is the effective change in U_{bi} due to vacuum-level shifts. The built-in potential U_{bi} was found to be equal to U_{soc}. N_i and W_{0V} are the ionized state density and the depletion width at zero bias, respectively.

surprisingly, two times lower than the one of double-layer cells (2%), even though the exciton dissociation efficiency in a co-deposited cell is supposed to be significantly higher due to the larger heterojunction interface. Others have reported similar observations for cells employing indium tin oxide as the anode material [14]. To understand the observed difference in the monochromatic external power conversion efficiency in more detail, one has to trace back the origin of the disparities in *FF*, *S* and U_{oc}.

7.2.1 Fill factor

The lower monochromatic η of photovoltaic cells based on co-deposited films is partly related to their lower *FF*. For efficient charge carrier read-out, both the donor and the acceptor phases are required to form a continuous network to allow bipolar charge transport. However, in the case of spatially distributed donor/acceptor heterojunctions, partial discontinuities in the donor and/or acceptor phases can occur. Furthermore, an increased energy level disorder in both phases due to strong intermixing of donor and acceptor materials may result in an increase of the charge carrier trap densities and, therefore, in a reduction of the electron and/or hole transport properties. Intuitively, it seems possible that this scenario holds true in the here-investigated bulk heterojunction photovoltaic cells, where the phase separation of the donor and the acceptor material is not optimized. If, as a consequence, the charge carrier transit times exceeded the lifetime of the charge carriers, charge carrier recombination and, hence, internal losses would be significant [15, 16], typically leading to a low *FF*. Moreover, space-charge built-up could determine the photoresponse of the cell, namely if blending resulted in strongly unbalanced charge carrier transport properties, favoring accumulation of the slower charge carrier species in the film. The resulting screening of the electric field dramatically affects the *FF* [15, 17]. In contrast to random blends, the *FF* of consecutively deposited cells was found to be higher, which demonstrates the superior transport properties of double-layer systems. However, the fill factors in MEH-OPV5/C_{60} blends may still be improved by tuning the film morphology as reported for other organic bulk heterojunction photovoltaic cells, in which an optimal phase separation allowed fill factors as high as 0.6 [5].

7.2.2 Photovoltaic sensitivity

In general, excitations created in the donor material within the exciton diffusion length from the heterojunction interface are susceptible for efficient exciton dissociation. Since the exciton diffusion length is typically shorter than the light absorption depth, a percolation of donor/acceptor heterojunctions is more efficient in terms of exciton dissociation than a conventional double-layer structure with a single planar donor/acceptor heterojunction. Very efficient photovoltaic cells using this kind of bulk heterojunction systems have been produced, shifting the performance of organic photovoltaic cell towards the one of their inorganic counterparts [5, 18].

Surprisingly, however, the saturated *S* of a co-deposited cell based on MEH-OPV5 and C_{60} was only two times higher than the one of a consecutively deposited cell (Fig. 7.2). This observation is in agreement with the findings of others, employing the same donor and acceptor materials, but a different anode [14].

In section 7.3, it will be demonstrated that the exciton diffusion length in MEH-OPV5 is in the 20 nm range, which makes a rather large volume fraction of the donor material in a consecutively deposited cell susceptible for exciton dissociation. However, from the results of section 7.3 and considering the architecture of the here-presented cells, it can be estimated that the photovoltaic sensitivity of a perfect bulk heterojunction cell should still exceed the one of a truly planar double-layer cell by one order of magnitude. To gain more insight into the relatively small increase in *S* upon changing the morphology from a double-layer to a percolated system, we therefore studied the topography of vacuum-deposited MEH-OPV5 on ITO/PEDOT:PSS substrates by atomic force microscopy (AFM) (Fig. 7.3). For comparison, the surface topographies of ITO and ITO/PEDOT:PSS were measured. While the ITO-coated substrate and the spin-coated PEDOT:PSS showed a rather smooth topography, the thermal vacuum deposition of MEH-OPV5 resulted in the formation of islands with an maximal height of about 40 nm and lateral extensions of around 200 nm. As a consequence, the area of the heterojunction interface of a consecutively deposited cell is larger than the one of an ideal double-layer cell, thereby approaching the area of a percolated system in terms of availability for exciton dissociation. Similar observations

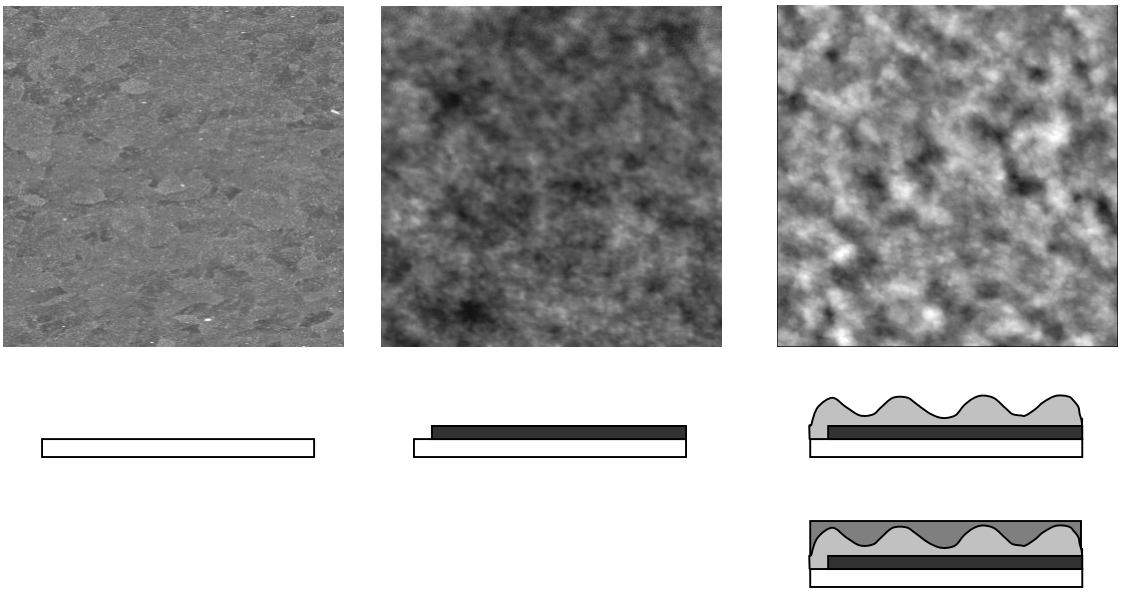

Figure 7.3 Topography of the ITO-coated glass substrate (left), spin-coated PEDOT:PSS on the ITO substrate (middle), and thermal vacuum-deposited MEH-OPV5 on PEDOT:PSS (right). All pictures are 2×2 µm. Maximal heights are from left to right: 20 nm, 15 nm, and 50 nm. Sketches below the pictures indicate the structure of the measured cells.

were reported by Ouali *et al.* [14], who studied the surface topography of vacuum-deposited MEH-OPV5 on mica. Likewise, they found that the consecutively deposited cell has an intermediate morphology between a blend and a truly planar double-layer film, exhibiting a finger-shaped interpenetrating pattern as indicated by the sketch in Fig. 7.3. Yet, the island formation of MEH-OPV5 deposited on PEDOT:PSS translates in a relative increase of the heterojunction interface of only 5 %, which cannot be exclusively responsible for the comparable photovoltaic sensitivities. In order to increase the heterojunction interface substantially, the average height of the topographic features needs to be close to the cell thickness d (~ 100 nm) and, concomitantly, their diameter is required to be much smaller than 200 nm, preferably in the range of the exciton diffusion length. Besides the increased heterojunction interface in a consecutively deposited cell due to roughness effects, a sub-optimal phase separation in the blend is even more likely to cause the similar exciton dissociation efficiencies, leading to the unveiled weak disparity in S.

7.2.3 Open circuit voltage

From Fig. 7.2 it can be seen that the U_{soc} of a double-layer cell came close to 0.9 V, while the one of a co-deposited cell was measured to be only 0.7 V. This difference in U_{soc} contributes to the disparity in the monochromatic η of consecutively and co-deposited cells. We also investigated the photovoltaic performance of single-layer MEH-OPV5 and C_{60} cells, respectively. The IV–characteristics in the dark and under illumination can be seen in Fig. 7.4. While the U_{soc} of a single-layer MEH-OPV5

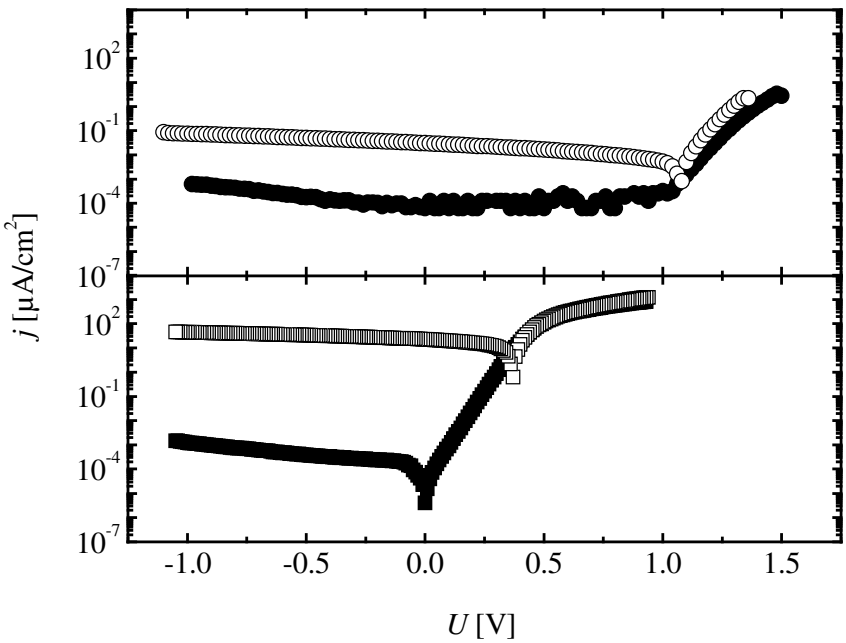

Figure 7.4 IV-characteristics of an ITO/PEDOT:PSS/MEH-OPV5/Al single-layer cell in the dark (●) and under illumination (○), and of an ITO/PEDOT:PSS/C_{60}/Al single-layer cell in the dark (■) and under illumination (□) with 1 mW/cm^2 at 458 nm.

cell approached 1.1 ±0.1 V (Table 2), the U_{soc} of a single-layer C_{60} cell was found to be only 0.3 ±0.2 V.

7.2.3.1 Built-in potential

Capacitance-voltage (CV) measurements on single-layer C_{60}, single-layer MEH-OPV5, double-layer and co-deposited cells revealed a bias-independent geometrical capacitance C_g at high frequencies (> 1 kHz). However, at low frequencies (< 100 Hz), a steep increase of the capacitance C in forward bias was observed for single-layer C_{60} and co-deposited cells (Fig. 7.5), while the capacitance of single-layer MEH-OPV5 and double-layer cells was hardly affected upon a change in bias.

Several models including Schottky contact, p-n junction, charging of surface states etc. predict such bias-dependent capacitance with slow dynamics. In the low frequency regime, a linear dependence of $1/C^2$ on bias reveals a depletion capacitance and simultaneously provides its built-in potential (U_{bi}), ionized state density (N_i), and the depletion width (W, e.g. at zero bias: W_{0V}):

Eq. 7.1

$$\frac{1}{C^2} = \left(\frac{W}{\varepsilon_s}\right)^2 = \frac{2}{q\varepsilon_s N_i}\left(U_{bi} - U\right)$$

where q is the electron charge, U is the applied voltage and ε_s is the semiconductor permittivity [19]. Similar to the photovoltaic measurements, the CV-measurements

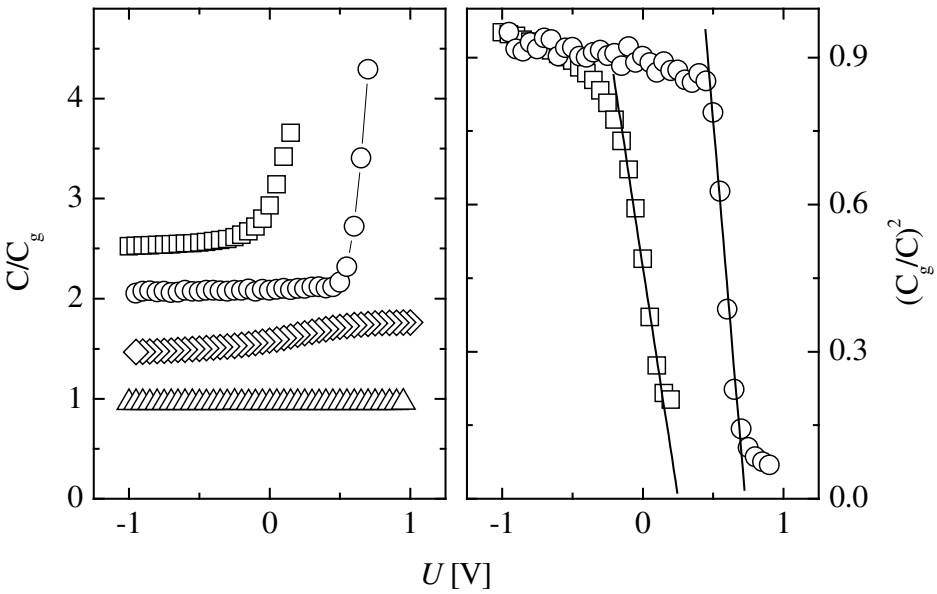

Figure 7.5 *Left*: Capacitance-voltage relation of a C_{60} single-layer cell (□), an MEH-OPV5 single-layer cell (Δ), a double-layer cell (◊), and a co-deposited cell (○) normalized on the geometrical capacitance C_g. Curves are shifted for clarity. *Right*: $(C_g/C)^2$ versus applied voltage of a single-layer C_{60} and a co-deposited cell.

showed strong deviations of U_{bi} from sample to sample and, consequently, also of W_{0V} and N_i. For each cell, however, the obtained U_{bi} was close to the measured U_{soc}. For single-layer C_{60} cells, $1/C^2$ versus U unveiled a depletion capacitance region only in a narrow range of forward bias when very thin layers of C_{60} were employed. At reverse bias, in contrast, the capacitance approached the geometrical capacitance (Fig. 7.5, Fig. 7.6). An increase in film thickness of C_{60} extended the depletion capacitance region towards reverse bias, corroborating a transition from a partly to a fully depleted cell (Fig. 7.6) and suggesting a one-side abrupt p-n heterojunction-type contact between C_{60} and one of the electrodes. Since a constant capacitance was observed over a wide range of bias and frequency for double-layer cells, the depletion layer was presumably formed at the anode/C_{60} contact. The energy diagrams of a partly and a fully depleted single-layer C_{60} cell are depicted in Fig. 7.6. We infer that the C_{60} layer is most likely n-doped with a rather low doping density of 10^{16} cm^{-3}. Although the origin of the doping is not known, Hayashi *et al.* demonstrated the formation of a Schottky barrier at C_{60}/metal interfaces by imaging the band bending with the Kelvin probe technique [20] and suggested a doping of C_{60} by intrinsic impurities.

Analogous to the observations in single-layer C_{60} cells, $1/C^2$ versus U in the low frequency regime of co-deposited cells showed a linear behavior in a narrow voltage range in forward bias, unveiling a depletion capacitance. The capacitance saturated to the geometrical capacitance in weak forward bias, which can be attributed to a transition from a partly to a fully depleted cell. Similar to single-layer C_{60} cells, the

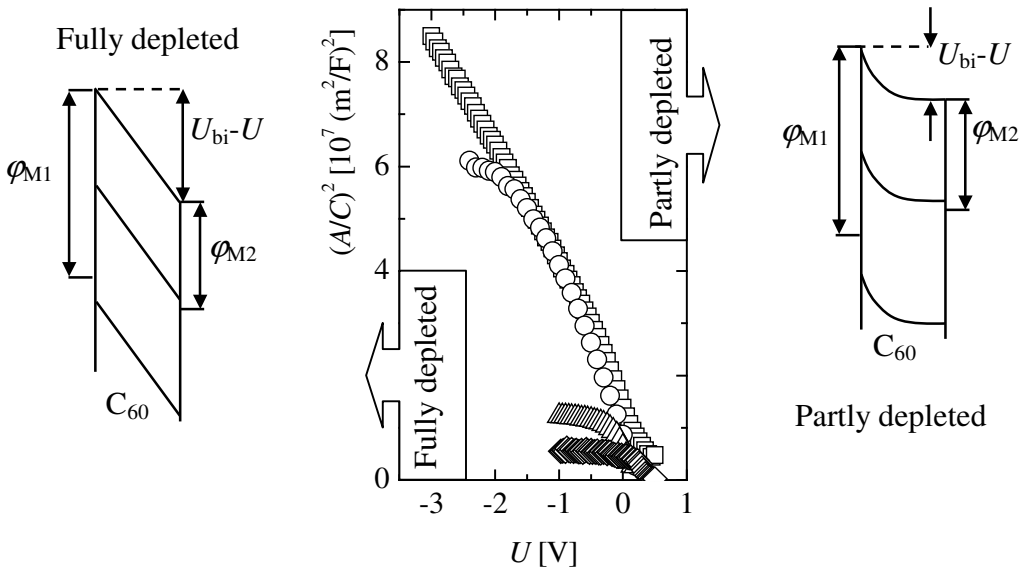

Figure 7.6 $(A/C)^2$ versus applied voltage for ITO/PEDOT:PSS/C_{60}/Al single-layer devices of 100 nm (◊), 130 nm (△), 300 nm (○), and 500 nm (□) thickness. A is the device area. The energy diagrams for fully and partly depleted conditions can be seen at the left and at the right side, respectively.

unveiled U_{bi} was always close to U_{soc}.

In conclusion, one-side abrupt p-n junctions were found to be present in single-layer C_{60} and co-deposited cells because of the use of slightly doped C_{60}. In turn, single-layer cells of MEH-OPV5 can be regarded to be fully depleted, since no depletion capacitance was observed. Moreover, it became apparent that for single-layer C_{60} and blended cells U_{bi} is a good approximation of U_{soc}.

7.2.3.2 Open circuit voltage and film structure

The major cell characteristics of the examined photovoltaic systems can be seen in Table 7.2. Assuming the metal-insulator-metal (MIM) model and typical workfunctions (φ) of PEDOT:PSS (5.2 eV) and Al (4.3 eV), the predicted U_{soc} for all cell-types should be about 0.9 V. We rationalize the lower U_{soc} found for single-layer C_{60} cells on basis of results obtained by ultraviolet photoelectron spectroscopy (UPS) that revealed strong vacuum-level shifts at metal/C_{60} interfaces (*Chapter 6*) [21], resulting in a low U_{bi}. Since the electron affinity of C_{60} (~ 4.4 eV) is approximately 0.1 eV below φ of Al, an electron transfer from Al to C_{60} is likely, pinning the LUMO of C_{60} to the Fermi-level of Al (δ_{AC} ~ 0.1 eV). Thus, a vacuum-level shift at the PEDOT:PSS/C_{60} interface (δ_{PC}) of about -0.5 eV would explain an U_{soc} of 0.3 V.

Similarly strong vacuum-level shifts were observed at metal/MEH-OPV5 contacts (*Chapter 6*) [22], which resulted in an U_{bi} of almost zero eV for Au/MEH-OPV5/Ag cells. The fact, however, that a single-layer ITO/PEDOT:PSS/MEH-OPV5/Al cell displayed an U_{soc} of 1.1 V (Table 7.2) shows that the formation of vacuum-level shifts at MEH-OPV5/electrode interfaces is strongly suppressed in terms of a reduction in U_{bi}. From *Chapter 4*, we know that the hole injection barrier at PEDOT:PSS/MEH-OPV5 contacts is approximately 0.4 eV. With an ionization potential of 5.3 eV for MEH-OPV5 (*Chapter 6*), a vacuum-level shift (δ_{PM}) of -0.3 eV is, hence, expected at the MEH-OPV5/PEDOT:PSS contact. Since we found U_{soc} = 1.1 V for single-layer MEH-OPV5 cells, a vacuum-level shift (δ_{AM}) of -0.5 eV must occur at Al/MEH-OPV5 contacts.

In a double-layer cell, an additional interface occurs, namely the donor/acceptor interface, and significant vacuum-level shifts (δ_{het}) at this heterojunction were previously unveiled [23]. Indeed, in order to obtain the U_{soc} of 0.9 V found for consecutively deposited cells (Table 7.2), a vacuum-level shift of 0.4 eV should exist at the heterojunction interface of C_{60} and MEH-OPV5. Yet, this is rather large if compared to vacuum-level shifts of 0.25 eV found at e.g. OPV5/C_{60} interfaces [23]. However, in a double-layer cell under illumination the accumulation of photoinduced charge carriers generated close to the planar heterojunction interface gives rise to a diffusion current that must be counterbalanced by a drift current at open circuit in order to yield zero current [24, 25]. The drift current requires an additional electric field, which is provided by an external voltage beyond the flat band condition. It has been shown that the open circuit voltage of double-layer cells might, therefore, even exceed the predictions of the MIM model by more than 1 V [24].

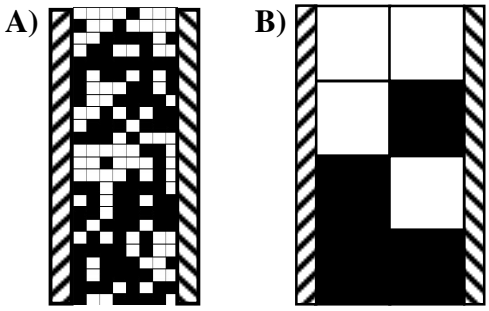

$$\delta U_{\mathrm{bi}}^{1} = \delta_{\mathrm{PM}} - \delta_{\mathrm{AM}}$$

$$\delta U_{\mathrm{bi}}^{2} = \delta_{\mathrm{PM}} - \delta_{\mathrm{AC}} + \delta_{\mathrm{het}}$$

$$\delta U_{\mathrm{bi}}^{3} = \delta_{\mathrm{PC}} - \delta_{\mathrm{AM}} - \delta_{\mathrm{het}}$$

$$\delta U_{\mathrm{bi}}^{4} = \delta_{\mathrm{PC}} - \delta_{\mathrm{AC}}$$

$$\left\langle \delta U_{\mathrm{bi}}^{\mathrm{blend}} \right\rangle = \tfrac{1}{2}\left(\delta_{\mathrm{C}} + \delta_{\mathrm{M}}\right)$$

Figure 7.7 Raster representation of a random blend of C_{60} (■) and MEH-OPV5 (□) sandwiched between PEDOT:PSS and Al (A). For an equally distributed blend, where both moieties and all patterns appear with the same probability, the system can be described by four general situations (B). $\left\langle \delta U_{\mathrm{bi}}^{\mathrm{blend}} \right\rangle$ is the spatially averaged change in U_{bi} that finally results from the vacuum-level shifts δ_{C} at the C_{60}/metal contacts and the vacuum-level shifts δ_{M} at the MEH-OPV5/metal contacts.

Our interpretation of the performance of co-deposited cells is mainly based on the assumption that the dipole strength at the metal/organic contacts and the ionized state density are proportional to the prevailing densities of organic materials. Since the ionized state density in MEH-OPV5 was zero, the N_i of a co-deposited film is solely determined by the volume fraction of C_{60} in the blend. As we deposited C_{60} and MEH-OPV5 in a ration of 1:1, the resulting N_{i} is consequently assumed to be half of the N_{i} determined for bare C_{60} films, while $W_{0\mathrm{V}}$ is roughly two times larger, as confirmed by CV measurements (Table 7.2).

Accordingly, we anticipated that the dipole strength δ is proportional to the surface density σ_{S} of the organic medium: $\delta \propto \sigma_{\mathrm{S}}$. The relation between U_{bi} of a blend and the unveiled vacuum-level shifts at the respective interfaces can be rationalized on basis of a schematic raster representation of a random blend as depicted in Fig. 7.7. In terms of vacuum-level shifts, the system can be reduced to four general situations. When MEH-OPV5 forms contact with both electrodes, such as it is depicted in the first line of Fig. 7.7 A and B, the vacuum-level shifts δ_{PM} and δ_{AM} contribute to U_{bi}, while vacuum-level shifts related to the heterojunctions between C_{60} and MEH-OPV5 (δ_{het}) compensate each other, resulting in a zero shift with respect to the heterojunctions. The same holds true when C_{60} is in contact with both electrodes. For situations where MEH-OPV5 forms contact with the anode, while C_{60} is in contact with the cathode and vice versa, the net-heterojunction vacuum-level shifts are $+\delta_{\mathrm{het}}$ and $-\delta_{\mathrm{het}}$, respectively. However, in a 1:1 random blend of MEH-OPV5 and C_{60}, all four situations statistically appear with the same frequency. Thus, in spatial average, solely the interfacial vacuum-level shifts at the metal/organic interfaces contribute to U_{bi} of cells based on

random blends, since the averaged vacuum-level shift related to the heterojunctions is zero.

With U_{soc} = 1.1 V of a single-layer MEH-OPV5 cell and an U_{soc} of 0.9 eV predicted by the metal-insulator-metal (MIM) model, the vacuum-level shifts at the metal/MEH-OPV5 interfaces increase the built-in potential by 0.2 eV. The interfacial MEH-OPV5 density in a blended cell, however, is half of the interfacial MEH-OPV5 density in a bare MEH-OPV5 cell, resulting in a dipole-layer strength of only 0.1 eV at the MEH-OPV5/metal interfaces. The same reasoning holds true for the C_{60}/metal interfaces in the blend. Since the vacuum-level shifts in a single-layer C_{60} cell change the U_{soc} by -0.6 eV, our assumption requires a vacuum-level shift contribution from the C_{60}/metal interfaces in the blend to be -0.3 eV. The predicted total vacuum-level shift is then -0.2 eV and U_{soc} of a co-deposited cell should be 0.7 V, which is in good agreement with the measured value (Table 7.2). Although requiring further verification, the proposed simple dilution model is useful to relate cell performance and morphology, since it predicts very accurately the effective ionized state density N_i, the saturated open circuit voltage U_{soc} (U_{bi}) and, consequently, the depletion width at zero bias W_{0V} for co-deposited photovoltaic cells as can be seen from Fig. 7.8.

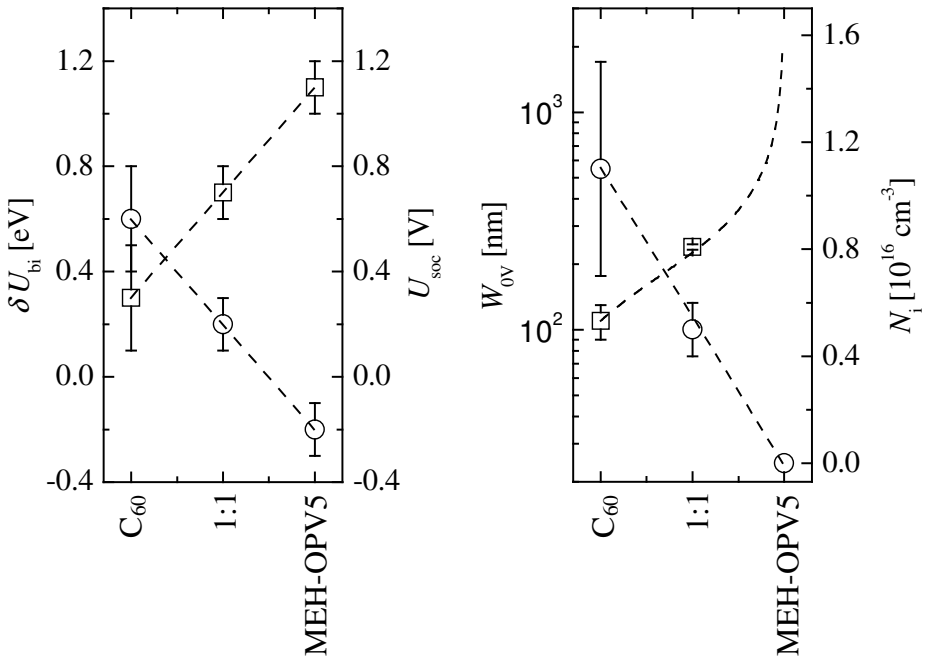

Figure 7.8 *Left*: The dipole layer strength (○) and the saturated open circuit voltage (□) versus the film composition of co-deposited systems, using MEH-OPV5 as donor and C_{60} as acceptor material. Dotted lines indicate the linear dependence on the material surface density. *Right*: The depletion width at zero bias (□) and the ionized state density (○) versus the film composition of co-deposited systems, using MEH-OPV5 as donor and C_{60} as acceptor. The dotted lines correspond to the predicted behavior, assuming the simple dilution model proposed in this study.

7.3 Action spectra and exciton diffusion

For many organic semiconductors, the relationship between the absorption spectrum and the spectral dependence of the photoresponse (action spectrum) can be classified as one of two types. If absorption and action spectra correlate well, i.e. the strongest absorption corresponds to the maximal photoresponse, the photoresponse is said to be *symbatic* to the absorption spectrum. Under other conditions, the spectrum is almost complementary, meaning that the minimum of the action spectrum occurs at the wavelength of strongest absorption. This behavior is termed *antibatic*. The normalized external quantum efficiency (EQE) and absorption spectra of double-layer cells based on the donors MEH-PPV, MEH-OPV5, and Ooct-OPV5 and the acceptor C_{60} are depicted in Fig 7.9. Substrates were maintained at room temperature during deposition. EQE spectra were measured under short circuit conditions and the samples were illuminated from the glass side, i.e. through the donor phase. Obviously, all EQE spectra of the investigated double-layer cells exhibited *antibatic* behavior at short circuit conditions, while bulk heterojunction photovoltaic cells typically show *symbatic* behavior [5]. Phenomenologically, we explain the *antibatic* behavior of the action spectra by the interplay of the pre-absorption of incident light in the donor phase, resulting in a weaker photon flux through the sensitive volume close to the donor/acceptor interface, with the exciton generation cross-section, which determines

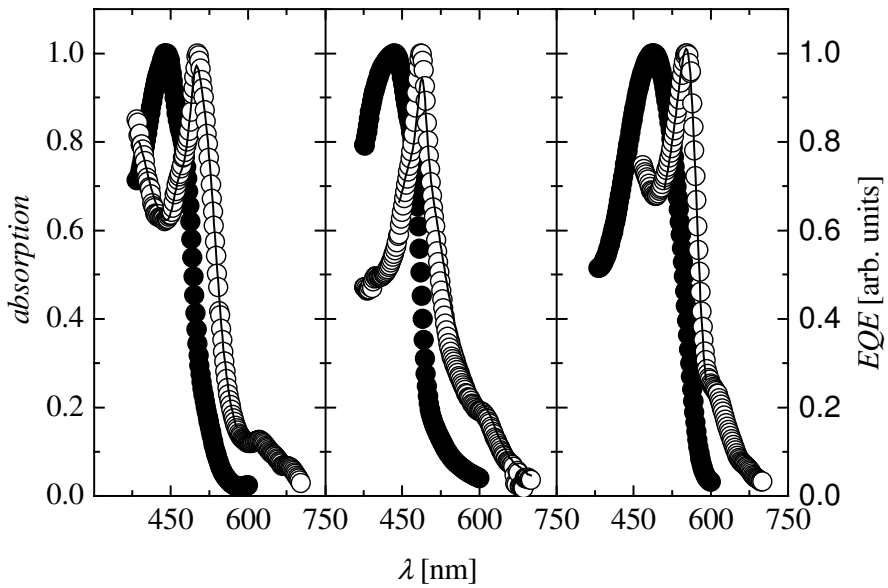

Figure 7.9 Normalized absorption (●) and action spectra (external quantum efficiency) (○) of double-layer photovoltaic cells with Ooct-OPV5 (130 nm) (left), MEH-OPV5 (105 nm) (middle), and MEH-PPV (100 nm) (right) as donor and C_{60} (~20 nm) as acceptor. The lines are fits using Eq. 7.4.

the number of generated excitons per photon. Since the extinction coefficient of C_{60} is small at the wavelengths of interest, we ignore photocurrents resulting from excitons generated in the C_{60} phase. The generation rate of excitons at the distance z from the anode upon an initial photon flux j_p is proportional to the photon flux $j_p Exp[-\alpha z]$ and the generation cross-section, which is characterized by the extinction coefficient α. Since almost all excitons within the exciton diffusion length L_e around the heterojunction interface dissociate, the rate of exciton dissociation is approximately given by $\int_{d-L_e}^{d} j_p \alpha Exp[-\alpha z] \partial z$. d is the thickness of the donor layer. The solution is $j_p Exp[-\alpha d](Exp[\alpha L_e]-1)$ and reduces for $\alpha L_e << 1$ to $j_p \alpha L_e Exp[-\alpha d]$. Thus, in the regime of very low absorption, the exciton generation cross-section becomes too small to result in strong exciton generation, even though the photon flux is high. The rate of exciton dissociation increases linearly with α. For stronger absorption, the rate of exciton dissociation is at its maximum and tends to decrease for even higher α, because the preabsorption of light reduces the photon flux through the active volume to such extend that even the large exciton generation cross-section does not allow significant exciton generation close to the heterojunction interface. As depicted in Fig. 7.10, EQE versus α, therefore, exhibited a bell-shaped form, with the maximal photoresponse being related to the thickness of the donor layer. The action spectra of non-optimized double-layer donor/acceptor photovoltaic cells are, hence, generally *antibatic*. In contrast, the exciton dissociation rate in a perfect blend can be approximated to $j_p(1-Exp[-\alpha d])$, and the maximum of the action spectrum coincides with the maximum of absorption.

For a more detailed analysis of the action spectra of double-layer cells, we derived the photovoltaic quantum efficiency, considering diffusive transport of excitons in the donor phase by solving the following steady-state continuity equation:

Eq. 7.2
$$0 = \frac{\partial n_e(z)}{\partial t} = g_e(z) - \frac{n_e(z)}{\tau} + D\frac{\partial^2 n_e(z)}{\partial z^2}$$

where $g_e(z)$ is the exciton generation rate, τ is the exciton lifetime, D is the exciton diffusion constant, and n_e is the density of excitons. The exciton generation rate is given by $g_e(z) \propto \alpha j_p Exp[-\alpha z]$. Interference of the incident light beam with back-reflected light, considering the actual device architecture, was ignored [26]. We regarded excitons to immediately dissociate via electron transfer from the donor to the acceptor when reaching the donor/acceptor interface, which results in the boundary condition $n_e(d) = 0$. Likewise, the boundary condition at the metal/donor interface was assumed to be $n_e(0) = 0$. This is justified, since excitons are quenched via energy transfer close to metal/organic interfaces. In first instance, we ignored the typical interaction distances for efficient charge and energy transfer. The photocurrent was taken to be proportional to the current j_e of excitons through the donor/acceptor interface:

Eq. 7.3

$$j_e = -D \left. \frac{\partial n_e(z)}{\partial z} \right|_{z=d}$$

The solution of Eq. 7.2 and Eq. 7.3 considering the assumed boundary conditions is:

Eq. 7.4

$$j_e = j_p \frac{L_e\alpha \left(\mathrm{Sinh}\left[\frac{d}{L_e}\right]^{-1} - \mathrm{Exp}[-\alpha d] \cdot \left(L_e\alpha + \mathrm{Coth}\left[\frac{d}{L_e}\right] \right) \right)}{(L_e\alpha)^2 - 1}$$

j_e is proportional to the incident photon flux j_p, and depends furthermore on the donor thickness d, the extinction coefficient α, and the exciton diffusion length L_e that is related to the diffusion coefficient and the exciton lifetime by $L_e^2 = D\tau$. Hence, by analyzing the action and the absorption spectra, and by knowing the thickness of the donor layer, one can gain information about the exciton diffusion length in the donor phase.

Assuming exciton diffusion in the donor-type material, the normalized EQE spectra could be modeled with Eq. 7.4 as depicted in Fig. 7.9 and 7.10. While d was determined by atomic force microscopy in tapping mode (TM-AFM), L_e was used as a free parameter. Reasonable fits could be obtained for action spectra from ITO/MEH-PPV/C_{60}/Al devices, requiring an exciton diffusion length in MEH-PPV of 7 ±4 nm.

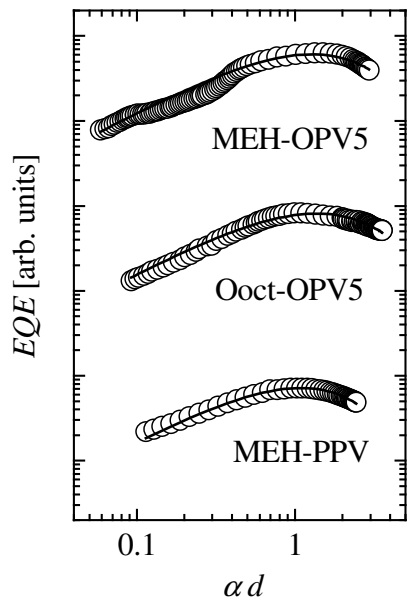

Figure 7.10 The normalized EQE versus the absorption cross-section α for double-layer photovoltaic cells with C_{60} as acceptor and Ooct-OPV5 (130 nm), MEH-OPV5 (105 nm), and MEH-PPV (100 nm) as donor. The lines are fits using Eq. 7.4. Curves are shifted for clarity.

This perfectly matches the exciton diffusion length reported for PPV by Halls *et al.* [26, 27] and is close to the one of MEH-PPV, which has been found to be 10-20 nm [28, 29]. Likewise, an L_e of 20 and 30 nm, respectively, was required to simulate the EQE spectra of double-layer cells based on MEH-OPV5 and Ooct-OPV5, which is considerably larger than that of MEH-PPV. Yet, from Fig. 7.10 it becomes apparent that the unveiled L_e of double-layer cells based on the investigated oligomers are only rough estimates, since the proposed diffusion model only partly predicts the observed EQE spectra. The mismatch of simulated and measured EQE spectra might result from the high surface roughness that is predominant in polycrystalline films. Light scattering, for instance, was clearly visible in this type of films, and the assumption that a simple exponential decay function describes the light intensity distribution in the sample is, hence, not valid.

The high surface roughness of the oligomeric thin films might, moreover, explain their larger L_e if compared to the polymer. In the used one-dimensional exciton diffusion model, L_e is determined by the assumption that double-layer cells are truly planar. Due to roughening of the heterojunction interface, which is predominant for cells based on Ooct-OPV5, this assumption is not fulfilled and the device thickness in Eq. 7.4 is a matter of distribution. However, the thickness variation, even for vacuum-deposited Ooct-OPV5 thin-films where the RMS film roughness is high, did not result in a considerable variation of the simulated action spectra. In addition, as discussed in section 7.2.2, the effective volume of exciton dissociation is increased if the heterojunction interface roughness is high and, hence, the deduced L_e is overestimated. One can estimate the discrepancy of measured and actual L_e by dilating the topographical map obtained by TM-AFM with a sphere of radius L_e as indicated in Fig. 7.11. It becomes apparent that the resulting L_e locally exceeds the factual L_e in regions of strong topographical variations, but yields an overestimation of L_e below 3 nm in spatial average. This is again a consequence of the fact that the diameter of the topological features exceeded the actual exciton diffusion length. Nonetheless, the unveiled disparity in L_e of the investigated donor materials correlates with their degree of crystallinity and might, hence, have its origin in differences in inter- and intramolecular organization, affecting the excitation lifetime and transport. It is likely that in highly disordered films of MEH-PPV exciton diffusion is suppressed, while in the tighter packed crystalline structures it is promoted. It has been, for example, reported that the exciton diffusion length in single crystals of anthracene is close to 50 nm [30], whereas the one in disordered films of PPV is below 10 nm [26, 27]. The low L_e found for MEH-PPV is partly related to its short excitation lifetime of 200-300 ps [8, 9]. With $L_e^2 = D\tau$ and an L_e of 7 nm , a diffusion constant in MEH-PPV of 2×10^{-7} m^2/s is obtained, which is not contradictory to previous results [8]. In contrast, however, an excitation lifetime of 1.2-1.7 ns [31] has been reported for vacuum-deposited thin films of Ooct-OPV5, which is considerably larger than the one of MEH-PPV. L_e in Ooct-OPV5 thin films is, hence, supposed to exceed that of MEH-PPV. Assuming an L_e of 30 nm for Ooct-OPV5 thin films, a diffusion constant of 5×10^{-7} m^2/s was estimated, comprehending a superior exciton transport in polycrystalline Ooct-OPV5 compared to disordered MEH-PPV thin films.

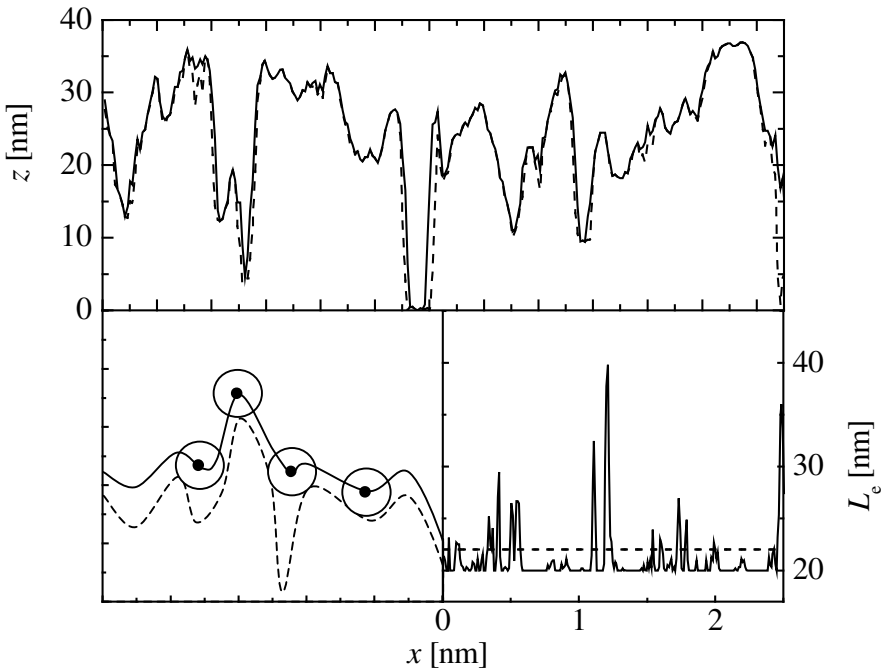

Figure 7.11 *Top*: Line scan (---) of the topographical map of Ooct-OPV5 deposited on PEDOT:PSS. Margins of the volume of efficient exciton dissociation determined by L_e (—). L_e was assumed to be 20 nm. *Left, bottom*: Schematic picture of the determination of the active volume in terms of exciton dissociation: excitons can diffuse in a sphere of radius L_e. (---) is a topographical line scan. (—) represents the limiting surface for efficient exciton dissociation. *Right, bottom*: Distributed L_e due to roughness effects (—) and spatial average of L_e (---).

7.4 A donor/acceptor block copolymer

Nowadays, the organization of donor and acceptor phases in bulk heterojunction photovoltaic cells is believed to be one of the technological challenges, which have to be tackled in order to bring organic photovoltaic cells closer to practical applications. Besides the fact that the lateral dimensions of donor and acceptor phases are required to be in the range of L_e, long-range order through the entire semiconducting film is essential for efficient charge carrier read-out. The establishment of phase separation in the nm-scale with long-range order, however, is not trivial, since the blending of two different molecular species usually results in a phase separation in the µm-scale with strong molecular intermixing and poor long-range correlation.

For the creation of the essential structural order in the donor/acceptor composite, the self-organization of block copolymers by micro-phase separation can be exploited [32-36]. The chemical link between the blocks of different chemical nature restricts the molecular ordering to the radius of gyration of the macromolecule, which typically is in the nm-range. The micro-phase separation of non-crystalline coil-coil

diblock copolymers is governed by the interaction enthalpy and the degree of polymerization, while the stability limit depends on the block length ratio. A variety of continuous and co-continuous two-phase morphologies, such as lamella, cylindrical or spherical morphologies have been observed. Certainly, the co-continuous morphologies have to be regarded as highly interesting for organic photovoltaic cells, since they provide a large heterojunction interface and, concomitantly, allow bipolar charge carrier read-out.

Tailoring of organic donor/acceptor phases by micro-phase separation can be achieved by implementing the donor and the acceptor functionality into different individual blocks. The functionalities can either be introduced into the backbone of the polymer block or into its sidechains. A donor/acceptor diblock copolymer with a conjugated PPV-like donor block (poly(1,4-(2,5-dioctyloxy)phenylene vinylene), DOO-PPV) and a coil-like copolymer block of styrene (S) and methylstyrene (MS) functionalized with C_{60} has been synthesized and extensively characterized [37-42]. In the frame of this work, we probed the establishment of micro-phase separation by TM-AFM. TM-AFM supplies information about the variations in the tip/surface interaction along the scanned area by investigating the phase change in the tip oscillation, thereby revealing the lateral distribution of regions with different chemical nature. In a simple picture, the rod-like DOO-PPV block can be regarded to be rigid compared to the flexible PS block, which results in a phase contrast between areas rich of PPV and areas mostly consisting of PS. Unfortunately, only information about the surface can be obtained and the spatial phase distribution remains inaccessible.

We investigated the topography and the phase contrast of thin films of DOO-PPV-b-P(S-stat-C_{60}MS) and of DOO-PPV-b-P(S-stat-ChloroMS) that was not functionalized with C_{60}. Both films were casted from chloroform on mica. Chloroform is a good solvent for both blocks, and self-organization in solution, such as micellization, should virtually not occur. The typical layer thickness was about 80 nm. While in both cases, the topography was rather smooth with a RMS roughness below 2 nm within the scanned area, phase contrast was clearly visible, suggesting a phase-separated morphology. The phase contrast maps revealed elongated features, but long-range order was not detectable in both cases. The elongated features in the DOO-PPV-b-P(S-stat-C_{60}MS) diblock copolymer exhibited a fairly uniform width of approximately 9 nm, which is comparable to the two-fold DOO-PPV block length of 4 nm. Phase contrast maps thus revealed a micro-phase separation in the range of the exciton diffusion length, a situation we intended to achieve in order to make the whole volume of the semiconducting layer sensitive for efficient exciton dissociation. The phase contrast maps, however, were not typical for micro-phase separated coil-coil-like block copolymers. The low molecular weight of the diblock copolymers, resulting in a weak phase segregation, and the rod-like character of the DOO-PPV block may explain the poor long-range ordering of the phase separation. Furthermore, each PS block embraced 28 methylstyrenes, while solely an average of 13 fullerenes were attached. Hence, bis-addition of two MS groups to each fullerene can be assumed. This observation suggests less flexible and, most likely, cross-linked polystyrene blocks that hinder the formation of micro-phases and may additionally reduce the solubility of the

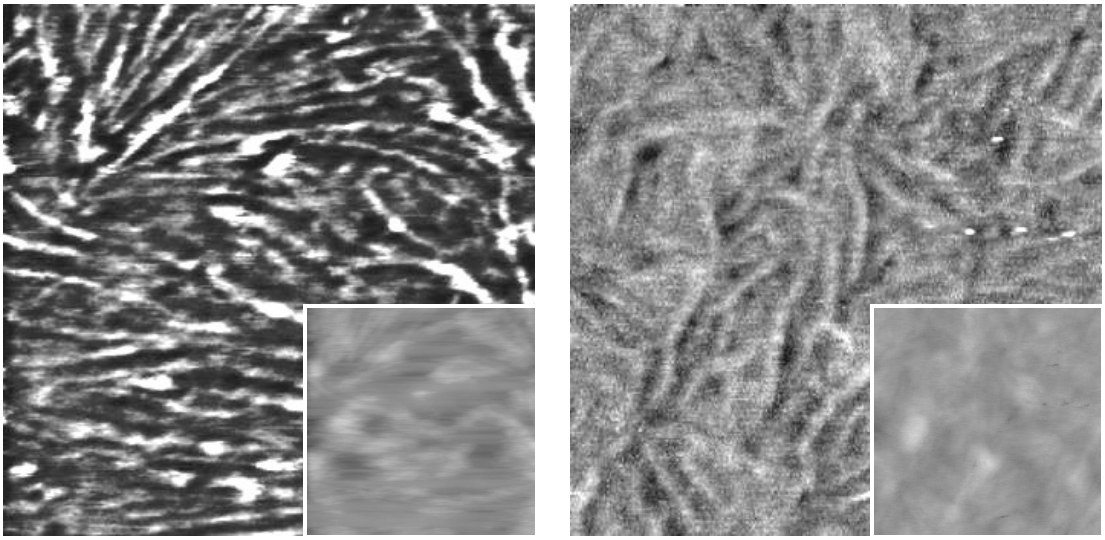

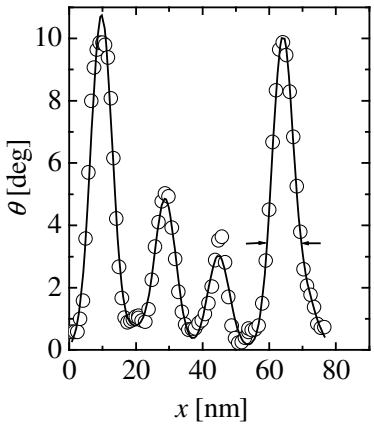

Figure 7.12 Topographical (*insert top*, 10 nm maximum) and phase contrast maps (*top*, 10 degree maximum) of thin films based on DOO-PPV-b-p(S-stat-C60MS) (400×400 nm) (left) and DOO-PPV-b-p(S-stat-ChloroMS) (right) (200×200nm). The width of the elongated features is about 9 nm (*bottom left*).

diblock copolymer in solvents like chloroform, toluene or dichlorobenzene. The poor processability and film-forming properties of the used diblock copolymer support this assumption.

The photovoltaic properties of cells based on the DOO-PPV-b-P(S-stat-C_{60}MS) diblock copolymer in an ITO/PEDOT:PSS/DOO-PPV-b-P(S-stat-C_{60}MS)/Al structure were compared to the ones of cells based on a blend of the DOO-PPV homopolymer and a statistical copolymer P(S-stat-C_{60}MS) in a 1:1 molar ratio. Both the diblock copolymer and the statistical copolymer P(S-stat-C_{60}MS) contained the same amount of C_{60} and the conjugation length of the DOO-PPV homopolymer was as long as the one of the DOO-PPV block in the block copolymer. Differences in the photovoltaic performance can, therefore, be attributed to morphological differences between the diblock copolymer and the blend. Both cells revealed a rather poor photovoltaic response (Fig. 7.13). The fact, however, that *S* of the diblock copolymer is much higher than of the blend justifies the use of block copolymers in photovoltaics. Even though the exciton dissociation interface is large in diblock copolymers, the weak long-range order and the narrow donor and acceptor phases may result in non-

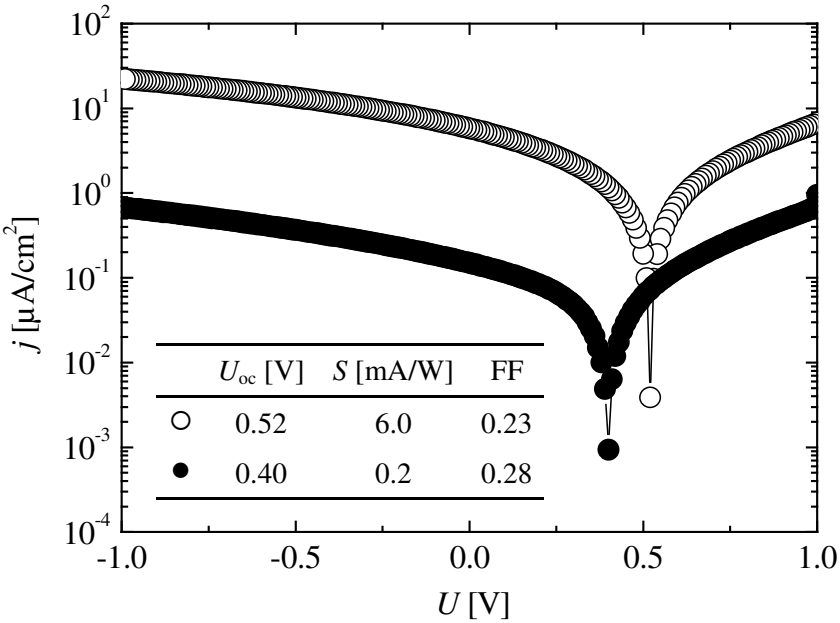

Figure 7.13 Photovoltaic response of a PPV-b-P(S-stat-C_{60}MS) donor/acceptor block copolymer (○) compared with a blend of the donor homo- and acceptor copolymer (●) under illumination at 458 nm with P_L = 1 mW/cm^2. The table summarizes the main photovoltaic characteristics.

continuous charge carrier transport paths throughout the semiconductor and in a high trap level density. These effects dramatically reduce the charge carrier transport properties and, therefore, the diode quality, which is reflected in the poor *FF*. In the blend, phase separation resulted in larger domains, and transport paths will most likely be semi-continuous, which demonstrates the importance of the mesoscopic phase organization. Optimization of the morphologies for both cases is, therefore, still required in order to give a conclusive answer to the question whether micro-phase separation results in a superior photovoltaic performance. Nonetheless, it is promising that a 30-fold increase in *S* could be achieved by replacing the blend of the donor and acceptor polymers by their corresponding block copolymer.

7.5 Conclusion

In this section, we reported on the influence of the thin-film morphology on the photovoltaic cell performance of donor/acceptor photovoltaic cells. The difference in monochromatic η between double-layer and co-deposited structures based on MEH-OPV5 and C_{60} could be rationalized in terms of charge carrier transport phenomena, interfacial effects, exciton diffusion, and morphology.

In particular, we found that the open circuit voltage in the investigated cells strongly depended on interfacial interactions, resulting in a lower U_{oc} in co- than in consecutively deposited cells. This was elucidated on basis of a simple dilution model,

which relates the open circuit voltage of co-deposited cells to interfacial interactions, taking the blend morphology into account.

From action spectra measurements, the exciton diffusion length for polymeric and oligomeric moieties could be estimated. An apparent increase of L_e with the degree of crystallinity was unveiled. We believe that the long exciton diffusion length found for MEH-OPV5 makes a large volume fraction of the donor material in double-layer cells susceptible for exciton dissociation, bringing S close to the one of blended cells. Concomitantly, a non-optimal phase separation in the blend can be assumed, contributing to the weak disparity in photovoltaic sensitivities that were found for co- and consecutively deposited photovoltaic cells. We discussed, furthermore, the influence of heterojunction roughness in double-layer systems on the accessible volume fraction for efficient exciton dissociation. Although a high surface roughness was unveiled, no substantially increased heterojunction interface could be confirmed. Hence, the increase in heterojunction interface due to surface roughness is regarded to be only secondarily responsible for the unveiled weak disparity in S between the two cell types. The relatively large S together with the higher open circuit voltage and superior diode behavior of the consecutively deposited cell, finally resulted in a higher monochromatic external power conversion efficiency than in a co-deposited cell.

The need for improved spatial distribution of donor and acceptor phases in a blend finally led us to use a donor/acceptor diblock copolymer, which exhibited a micro-phase separation in the nm-range. Even though the photovoltaic performance was generally weak, we found that the photovoltaic sensitivity of the diblock copolymer significantly exceeded the one of a blend of the corresponding homopolymers, which demonstrates the potential of functionalized block copolymers in the field of organic photovoltaic cells.

References

[1] J. J. M. Halls, C. A. Walsh, N. C. Greenham, E. A. Marseglia, R. H. Friend, S. C. Moratti and A. B. Holms, Nature **376**, 498 (1995).

[2] G. Yu, J. Gao, J. C. Hummelen, F. Wudl and A. J. Heeger, Science **270**, 1789 (1995).

[3] M. Granström, K. Petritsch, A. C. Arias, A. Lux, M. R. Anderson and R. H. Friend, Nature **395**, 257 (1998).

[4] L. S. Roman, W. Mammo, L. A. A. Petterson, M. R. Andersson and O. Inganäs, Adv. Mater. **10**, 774 (1998).

[5] S. E. Shaheen, C. J. Brabec, N. S. Sariciftci, F. Padinger, T. Fromherz and J. C. Hummelen, Appl. Phys. Lett. **78**, 841 (2001).

[6] A. Goetzberg and C. Hebling, Solar Energy Materials & Solar Cells **62**, 1 (2000).

[7] E. L. Frankevich, A. A. Lymarev, I. Sokolik, F. Karasz, S. Blumstengel, S. Baughman and H. H. Hörhold, Phys. Rev. B **46**, 9320 (1992).

[8] M. Gailberger and H. Bässler, Phys. Rev. B **44**, 8643 (1991).

[9] H. Becker, A. Lux, A. B. Holmes and R. H. Friend, Synth. Met. **85**, 1289 (1997).

[10] N. S. Sariciftci, L. Smilowitz, A. J. Heeger and F. Wudl, Science **258**, 1474 (1992).

[11] C. W. Tang, Appl. Phys. Lett. **48**, 183 (1986).

[12] P. Peumans and S. R. Forrest, Appl. Phys. Lett. **79**, 126 (2001).

[13] C. Melzer, V. V. Krasnikov and G. Hadziioannou, Appl. Phys. Lett. **82**, 3101 (2003).

[14] L. Ouali, V. V. Krasnikov, U. Stalmach and G. Hadziioannou, Adv. Mater. **11**, 1515 (1999).

[15] A. M. Goodman and A. Rose, J. Appl. Phys. **42**, 2823 (1971).

[16] V. D. Mihailetchi, J. A. Knoster and P. W. M. Blom, *to be published* (2004).

[17] C. Melzer, E. J. Koop, V. D. Mihailetchi and P. W. M. Blom, Adv. Funct. Mater. (2004), *accepted*.

[18] T. Munters, T. Martens, L. Goris, V. Vrindts and J. Manca, Thin Solid Films **403-404**, 247 (2002).

[19] S. M. Sze, *Physics of Semiconductor Devices*, Wiley & Sons Inc., New York (1981).

[20] N. Hayashi, H. Ishii, Y. Ouchi and K. Seki, J. Appl. Phys. **92**, 3784 (2002).

[21] S. C. Veenstra, A. Heeres, G. Hadziioannou, G. A. Sawatzky and H. T. Jonkman, Appl. Phys. A: Mater. Sci. Proc. **75**, 661 (2002).

[22] S. C. Veenstra, U. Stalmach, V. V. Krasnikov, G. Hadziioannou, H. T. Jonkman, A. Heeres and G. A. Sawatzky, Appl. Phys. Lett. **76**, 2253 (2000).

[23] *Thesis:* S. C. Veenstra, *Electronic Structure of Molecular Systems. From Gas Phase to Thin Films to Devices*, Polymer Chemistry Rijksuniversiteit Groningen, Groningen (2002).

[24] C. M. Ramsdale, J. A. Baker, A. C. Arias, J. D. MacKenzie, R. H. Friend and N. C. Greenham, J. Appl. Phys. **92**, 4266 (2002).

[25] J. A. Baker, C. M. Ramsdale and N. C. Greenham, Phys. Rev. B **67**, 075205 (2003).

[26] J. J. M. Halls, K. Pichler, R. H. Friend, S. C. Moratti and A. B. Holms, Appl. Phys. Lett. **68**, 3120 (1996).

[27] J. J. M. Halls, K. Pichler, R. H. Friend, S. C. Moratti and A. B. Holmes, Synth. Met. **77**, 277 (1996).

[28] T. J. Savenije, J. M. Warman and A. Goossens, Chem. Phys. Lett. **287**, 148 (1998).

[29] L. Smilowitz, A. Hays, A. J. Heeger, G. Wang and J. E. J. Bowers, J. Chem. Phys. **98**, 6505 (1993).

[30] M. D. Cohen, E. Klein and Z. Ludmer, Chem. Phys. Lett. **37**, 611 (1976).

[31] *Thesis:* H. J. Brouwer, *Semiconducting Polymers for Light-Emitting Diodes and Lasers*, Polymer Chemistry Rijksuniversiteit Groningen, Groningen (1998).

[32] E. Helfand and Z. R. Wassermann, *Development in Block Copolymers-1*, Applied Science Publisher, New York (1982).

[33] F. S. Bates and G. H. Fredrickson, Annu. Rev. Phys. Chem. **41**, 525 (1990).

[34] F. S. Bates, Science **251**, 898 (1991).

[35] T. P. Lodge and M. J. Muthukumar, Phys. Chem. **100**, 13275 (1996).

[36] S. I. Stupp, V. Le Bonheur, K. Walker, L. S. Li, K. E. Huggins, M. Keser and A. Amstutz, Science **276**, 384 (1997).

[37] U. Stalmach, B. de Boer, C. Videlot, P. F. van Hutten and G. Hadziioannou, J. Am. Chem. Soc. **122**, 5464 (2000).

[38] B. de Boer, U. Stalmach, H. Nijland and G. Hadziioannou, Adv. Mater. **12**, 1581 (2000).

[39] U. Stalmach, B. de Boer, A. D. Post, P. F. van Hutten and G. Hadziioannou, Angew. Chem. Int. Ed. **40**, 428 (2001).

[40] B. de Boer, U. Stalmach, P. F. van Hutten, C. Melzer, V. V. Krasnikov and G. Hadziioannou, Polymer **42**, 9097 (2001).

[41] B. de Boer, U. Stalmach, C. Melzer and G. Hadziioannou, Synth. Met. **121**, 1541 (2001).

[42] *Thesis:* B. de Boer, *Design, Synthesis, Morphology and Properties of Semiconducting Block Copolymers for Photonic Applications*, Polymer Chemistry Rijksuniversiteit Groningen, Groningen (2001).